

Thickness-Dependent Microstructural Evolution of CsPbBr₃ Nanobricks Induced by Electron Beam Irradiation

Feiyu Diao, Qingye Zhang, Jiaju Wang, Wenshuang Liang, Federico Rosei, Xuyan Xue,* and Yiqian Wang*

All-inorganic halide perovskites exhibit exceptional optical properties and are promising photoactive materials for optoelectronics. However, their stability remains a key challenge, exacerbated by a limited understanding of degradation mechanisms. Herein, *in situ* transmission electron microscopy (TEM) is used to investigate the effect of thickness on the structural stability of CsPbBr₃ nanobricks under electron beam irradiation. CsPbBr₃ nanobricks with different thicknesses have been prepared using a traditional hot-injection method, giving rise to a distinctive cubic structure. A modulated structure, caused by bromine vacancy ordering, has been observed in the thin nanobricks. The degradation behaviors of nanobricks are related to thickness-dependent bromine vacancy formation in the CsPbBr₃ lattice. More bromine vacancies exist in thin nanobricks than thick ones, resulting in a greater number of undercoordinated Pb atoms which accelerate irradiation-induced degradation. Decomposition products include Pb nanoparticles, which also demonstrate thickness-dependent characteristics. TEM images of Pb nanoparticles formed from thin nanobricks show evidence of irradiation-induced amorphization. In thicker nanobricks, Pb nanoparticle size increases with the duration of electron beam irradiation, while the remaining Cs atoms bond with Br atoms to form relatively stable CsBr nanoparticles. These results contribute to understanding of degradation mechanisms in cesium lead halide perovskites under electron beam irradiation.

the discrete electronic energy states of CsPbX₃ can be tuned by adjusting the size, shape, and chemical composition of nanocrystals.^[2–4] Despite intensive studies on their preparation and applications,^[5–8] CsPbX₃ materials exhibit inherent structural instability when exposed to moisture, heat, or various forms of irradiation.^[9–11] While device encapsulation can mitigate humidity-induced damage, it falls short in safeguarding against thermal and irradiation-induced degradation. Particularly in space solar cells, CsPbX₃ materials encounter significant stability issues when subjected to electron, X-ray, and photon irradiation. Currently, the precise mechanism underlying the photoinduced degradation process remains elusive.^[12] An in-depth understanding of damage mechanisms in CsPbX₃ under different stimuli, particularly light irradiation, is needed to facilitate stability improvements and enable commercial applications.


Some investigations propose that photoinduced degradation may arise from electron bombardment during ionization processes.^[13] Others indicate that the

generation of substantial photocurrents under short-circuit conditions induces the formation of additional trap states, subsequently deteriorating the performance of perovskite solar cells.^[14] Manifestly, electrons play a pivotal role in the degradation of CsPbX₃ nanomaterials. High-resolution transmission electron microscopy (HRTEM) provides an ideal method for *in situ* characterization of structural stability and transformation

1. Introduction

Cesium lead halide perovskites (CsPbX₃, X = Cl, Br, I) are a widely studied class of materials with unique optoelectronic properties. Of particular interest are a high absorption coefficient, high carrier mobility, narrow photoluminescence emission, and a high luminescence efficiency.^[1] In addition,

F. Diao
Industrial Research Institute of Nonwovens & Technical Textiles
Shandong Engineering Research Center for Specialty Nonwoven Materials
College of Textile and Clothing
Qingdao University
No. 308 Ningxia Road, Qingdao 266071, P. R. China

 The ORCID identification number(s) for the author(s) of this article can be found under <https://doi.org/10.1002/ssstr.202300577>.

© 2024 The Authors. Small Structures published by Wiley-VCH GmbH. This is an open access article under the terms of the Creative Commons Attribution License, which permits use, distribution and reproduction in any medium, provided the original work is properly cited.

DOI: 10.1002/ssstr.202300577

F. Diao, Q. Zhang, J. Wang, W. Liang, X. Xue, Y. Wang
College of Physics & State Key Laboratory
Qingdao University
No. 308 Ningxia Road, Qingdao 266071, P. R. China
E-mail: xuexy@qdu.edu.cn; yqwang@qdu.edu.cn

F. Rosei
Centre Énergie Matériaux et Télécommunications
Institut National de la Recherche Scientifique
1650 Boulevard Lionel-Boulet, Varennes, Québec J3X 1P7, Canada

behaviors in CsPbX₃ nanomaterials. The high-energy electron beam (EB) in HRTEM can be used as a controllable irradiation source to induce the degradation of CsPbX₃ nanomaterials while simultaneously imaging microstructural transformations in real time. This technique is frequently used to characterize beam-induced changes in radiosensitive materials, including morphological transformations, phase transitions, mass loss, and defect formation.^[15–17] In the case of halide perovskites, degradation induced by the EB can cause formation of nanoparticles, which give high image contrast in transmission electron microscopy (TEM). Some researchers have claimed that these nanoparticles are made of Pb,^[18] while others suggest that they are PbX₂, CsX, or CsPb.^[19,20] Such discrepancies reflect that the degradation mechanism remains controversial for CsPbX₃ under electron irradiation, which might be caused by different operating conditions in TEM and the intrinsic properties of CsPbX₃.

Interactions between electron and specimen in an electron microscope predominantly include knock-on collisions and radiolysis, depending on the operation conditions.^[15,21,22] Knock-on damage is dominant at high incident electron energy (i.e., 200 keV), resulting in an irreversible displacement of atoms and defect formation. Radiolysis occurs mainly at lower incident electron energy (i.e., 80 keV), which is caused by inelastic scattering accompanied by a strong thermal effect. Manna et al.^[22,23] investigated the influence of TEM operating conditions (including incident electron energy, irradiation dose rate, and temperature) on the transformation behavior of CsPbBr₃ nanosheets with a thickness of 3 nm. Radiolysis was found to be the dominant damage mechanism, and the degradation process was accompanied by desorption of halogen species and the nucleation of metallic Pb particles. It was also found that a low surface-to-volume ratio helped to prevent irradiation-induced damage. Nevertheless, the influence of nanoparticle size on the structure and stability of CsPbBr₃ is not well understood. Size, especially thickness, is known to play a prominent role in determining the optical properties of perovskite materials.^[24–28] Therefore, it is important to investigate the structural stability of different CsPbX₃ thicknesses under EB irradiation.

Here, we report the synthesis of CsPbBr₃ nanobricks with different thicknesses, and their transformation behaviors are induced by EB irradiation. Thick nanobricks are found to be more robust than thin nanobricks. The rapid degradation of thin nanobricks is attributed to intrinsic bromine vacancies which provide more undercoordinated Pb atoms with decreased diffusion energy. The presence of bromine vacancies inside CsPbBr₃ is demonstrated by both TEM imaging and density functional theory calculations. Crystal defects including dislocations, stacking faults, and twinning are generated to release excess energy during the formation process of Pb nanoparticles.

2. Results and Discussion

2.1. Structure Identification of CsPbBr₃ Nanobricks

Figure 1a displays a typical bright-field (BF) TEM image of as-synthesized and undamaged CsPbBr₃ nanobricks, showing cuboid morphologies with nonuniform edge lengths.

Statistical analysis of 240 nanobricks produced a distribution of edge lengths ranging from 30 to 120 nm with an average value of 60 nm. Both atomic force microscopy (AFM) (Figure S1 and S2, Supporting Information) and electron energy-loss spectroscopy (EELS) (Figure S3, Supporting Information) measurements suggest that thin nanobricks have thicknesses between 10 and 20 nm, whereas thick nanobricks have thicknesses between 50 and 60 nm. TEM contrast differences seen in Figure 1a,b are thought to originate mainly from nanobrick thickness variation. Figure 1b shows a typical HRTEM image, corresponding to a region of Figure 1a (enclosed by a white rectangle) which includes both thick (I) and thin (II) nanobricks. Crystal lattice spacings can be measured directly from Figure 1b. For nanobrick I, the lattice spacing is 2.92 Å; nanobrick II has a slightly smaller spacing of 2.88 Å. A modulated structure with a periodicity of approximately 5.76 Å can also be observed, which is further corroborated by the intensity distribution extracted from the magnified HRTEM image in Figure 1c.

To determine whether these lattices originate from a cubic phase ($a = 5.83$ Å) or an orthorhombic phase ($a = 8.207$ Å, $b = 8.255$ Å, $c = 11.759$ Å), we carried out detailed analysis of SAED patterns acquired from thick nanobrick I and thin nanobrick II, shown in Figure 1d,e, respectively. These patterns are rotated by an angle of $\approx 39^\circ$ with respect to the HRTEM image in Figure 1b. The SEAD pattern in Figure 1d is in good agreement with the simulated electron diffraction pattern for cubic CsPbBr₃ in Figure 1f. The measured spacing of 2.92 Å in the nanobrick I (Figure 1b) corresponds to {200} planes in simulated cubic CsPbBr₃. However, the (220), (2-20), and (004) planes of an orthorhombic CsPbBr₃ also have a lattice spacing of ≈ 2.9 Å. To exclude the presence of an orthorhombic phase, we simulated electron diffraction along the [001] zone-axis of an orthorhombic CsPbBr₃, as shown in Figure 1g. Compared to the experimental SEAD pattern in Figure 1d, the simulated pattern shows additional diffraction spots marked by purple circles. This suggests that thick nanobrick I has a cubic, rather than orthorhombic, crystal structure. For nanobrick II, the SEAD pattern in Figure 1e contains superlattice spots (indicated by white arrows) in the midway between primary diffraction spots along the [010] direction in addition to the primary diffraction spots of the cubic phase. This SEAD pattern has the potential to cause confusion, as similar diffraction patterns have apparently been obtained from an orthorhombic phase viewed along [110] direction.^[29,30] It should be noted that the majority of existing diffraction analysis^[29–31] of the orthorhombic phase has been performed from fast Fourier transforms (FFTs) of HRTEM images, and various reports have shown intensity variations of diffraction spots in the FFTs.^[29,31] No experimental SEAD patterns, like that of Figure 1e, have previously been obtained. To further clarify the origin of superlattice spots, we have simulated the [110] zone-axis diffraction pattern for orthorhombic CsPbBr₃, shown in Figure 1h. Although the simulated distribution of diffraction spots is similar to the observed SEAD pattern (Figure 1e), some experimentally observed superlattice spots are extinct in the middle row (enclosed by orange dash lines in Figure 1f), while other simulated superlattice spots differ in intensity from experimental observation (e.g., the regions enclosed by green dash lines in Figure 1f). This suggests that the superlattice spots observed in Figure 1e stem from a modulated structure in the cubic phase

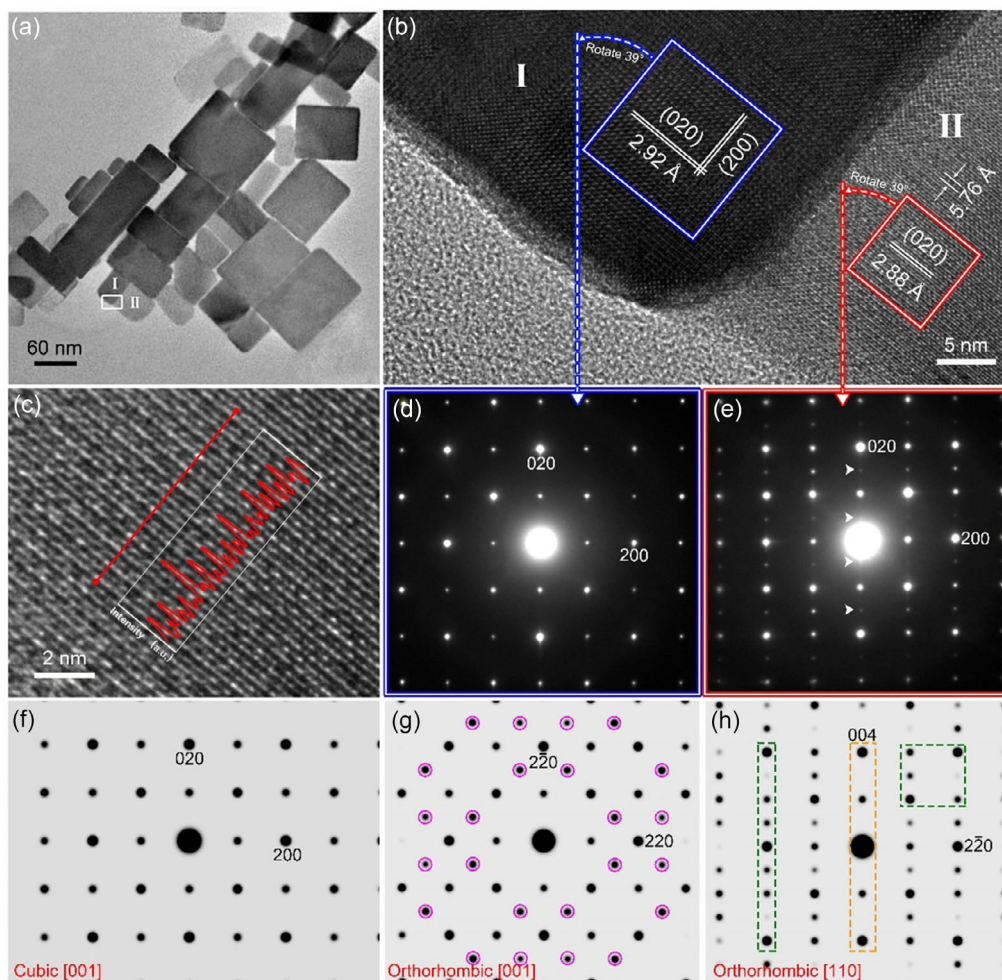


Figure 1. a) Typical BF TEM image of CsPbBr₃ nanobricks; b) typical HRTEM image of nanobrick I and II; c) enlarged HRTEM image of nanobrick II with an inset showing intensity variation along the red line; d) selected-area electron diffraction (SAED) patterns acquired from nanobrick I and e) nanobrick II; f) simulated electron diffraction patterns of cubic CsPbBr₃ along the [001] zone axis and g) orthorhombic CsPbBr₃ along the [001] and h) [110] zone axes.

rather than the orthorhombic phase of CsPbBr₃. Previous studies^[32–34] have demonstrated that a cubic phase of CsPbBr₃ can be obtained at reaction temperatures above 150 °C. Our synthesis temperature reaches ≈200 °C, and cubic CsPbBr₃ nanobricks form, which is consistent with previous findings. Moreover, previous investigation^[35] has reported a phase transition from a cubic to an orthorhombic structure for CsPbBr₃ nanoparticles when their size surpasses 10 nm. This contradicts our findings because both thick and thin nanobricks are larger than 10 nm, but have a cubic structure.

Previous reports^[36–38] suggested that modulated structures in perovskite oxide materials can originate from cation ordering, spin ordering, or oxygen vacancy ordering. Cation ordering^[36] is a major cause of modulated structures in perovskite oxide materials doped with alkaline earth metals; spin ordering^[37] modulated structures usually occur in ferromagnetic materials; oxygen-vacancy ordering^[38] is very common in perovskite oxide materials. However, to the best of our knowledge, a modulated structure has not previously been observed in cesium lead bromide perovskite materials. Compared with traditional perovskite

oxides, Br atoms in CsPbBr₃ occupy O atomic sites at the vertices of PbBr₆^{4–} octahedra. Thus, we hypothesize that the modulated structure observed in thin nanobricks is associated with bromine vacancy ordering in CsPbBr₃. To test this hypothesis, we acquired EDS spectra from both thick and thin nanobricks, as shown in Figure 2a,b. Spectral quantification shows that the atomic ratio for Cs, Pb, and Br in thick nanobricks is 1:1:2.98, whereas for thin nanobricks it is 1:1:2.75. In addition, elemental quantification analysis of other nanobricks (Table S1, Supporting Information) demonstrates that thin nanobricks have a much lower bromine content than thick ones. It has been reported that the surface termination of CsPbBr₃ crystals is induced by Cs–Br interactions.^[39,40] Considering the higher specific surface area of thin nanobricks, their percentage bromine content should be much higher than that of thick nanobricks. However, the observed trend contradicts this expectation. Therefore, it can be inferred that there are abundant bromine vacancies in the thin nanobricks, and the ordered arrangement of these vacancies leads to structural modulation. Moreover, EELS is performed to further confirm the presence of Br vacancies in the thin

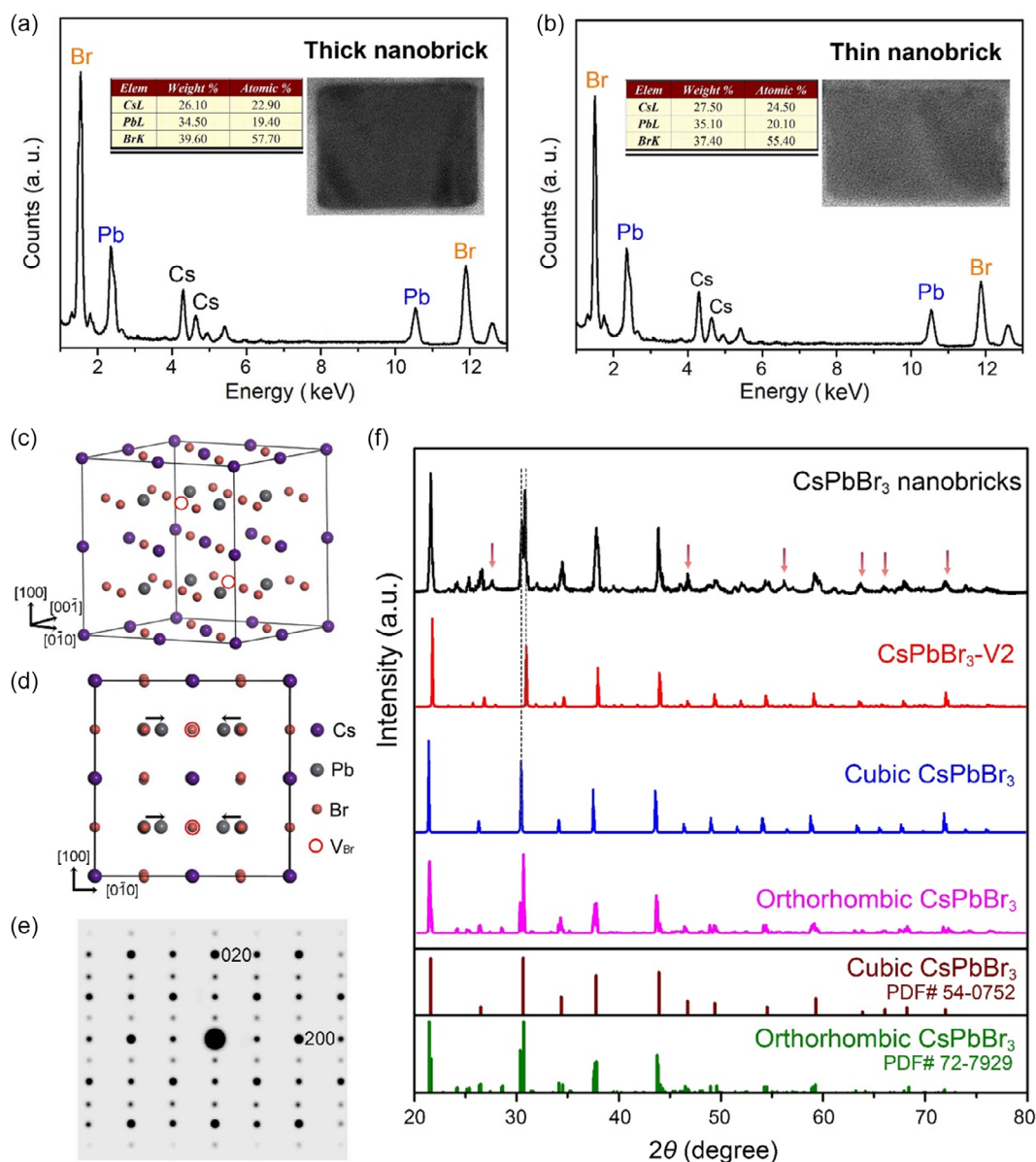


Figure 2. Energy dispersive X-ray spectroscopy (EDS) spectra acquired from a) thick and b) thin nanobricks; c) atomic model of CsPbBr₃-V2; d) top-down view of the CsPbBr₃-V2 atomic model; e) simulated electron diffraction pattern of CsPbBr₃-V2; f) X-ray diffractometer (XRD) pattern acquired from CsPbBr₃ nanobricks (black line), the computed powder diffraction (CPD) patterns of CsPbBr₃-V2 (red line), cubic CsPbBr₃ (blue line), and orthorhombic CsPbBr₃ (purple line) models.

nanobricks. Figure S4 (Supporting Information) shows the EELS spectra of Br M_{4,5} edges acquired from both thick and thin nanobricks. As depicted in Figure S4 (Supporting Information), the peak intensity of Br M_{4,5} acquired from the thin nanobrick is lower than that from the thick one, indicating the presence of Br vacancies in the thin nanobricks, consistent with the observation of oxygen vacancies in α -Fe₂O₃.^[41] In addition, the presence of Br vacancies in the thin nanobrick induces changes in the valence state of Br, leading to a more pronounced shoulder peak at ≈ 65 eV.

Density functional theory (DFT) calculations and electron diffraction simulations were performed to further verify the origin

of structural modulation. ($2 \times 2 \times 2$) supercells (Cs₈Pb₈Br₂₄) were used to build CsPbBr₃ atomic models with bromine vacancies. By considering the orientation of bright and dark stripes observed in our HRTEM images, we determined that bromine vacancies in our CsPbBr₃ atomic models should be ordered along the [010] direction. We built a series of CsPbBr₃ atomic models with different numbers of bromine vacancies, while still maintaining the integrity of the crystal structure. These include CsPbBr₃ (without any bromine vacancies), CsPbBr₃-V1 (one bromine vacancy), CsPbBr₃-V2 (two bromine vacancies), CsPbBr₃-V3 (three bromine vacancies), and CsPbBr₃-V4 (four bromine vacancies). Figure 2c,d shows the atomic models of CsPbBr₃-V2;

the rest of the models are shown in Figure S5 (Supporting Information). Figure 2e presents a simulated electron diffraction pattern from CsPbBr₃-V2. The simulated pattern in Figure 2e is in good agreement with the SAED pattern acquired from nanobrick II (Figure 1e), suggesting that CsPbBr₃-V2 matches the real crystal structure of nanobrick II. In addition, after structural optimization, we find that Pb atoms adjacent to bromine vacancies are pushed closer to each other. This relaxation of nearby Pb atoms toward vacancies can be seen in the top-down view of the CsPbBr₃-V2 model (Figure 2d). It is reasonable to conclude that bromine vacancy ordering along the [010] direction is responsible for the structure modulations found in nanobrick II, and that a resultant contraction in Pb–Pb interatomic distances leads to the decreased (020) interplanar spacing observed in the thin nanobrick (Figure 1d). This observation is supported by the XRD results from as-synthesized CsPbBr₃ nanobricks and the CPD patterns of cubic CsPbBr₃, CsPbBr₃-V2, and orthorhombic CsPbBr₃ models, as depicted in Figure 2f. In the XRD pattern, we see numerous splitting peaks in addition to the characteristic peaks of cubic CsPbBr₃. Careful examination reveals that the experimental XRD pattern encompasses all peaks observed in the CPD pattern of CsPbBr₃ and CsPbBr₃-V2, suggesting the presence of different phases within the synthesized CsPbBr₃ nanobricks. Coexistence of stoichiometric CsPbBr₃ (thick nanobricks) and nonstoichiometric CsPbBr_{2.75} (thin nanobricks) can account for the splitting peaks observed in the experimental XRD pattern. Although the double peaks appearing at $\approx 30^\circ$ are typically considered characteristic of the orthorhombic CsPbBr₃,^[42] a detailed analysis of Figure 2f reveals several discrepancies between our results and the standard orthorhombic CsPbX₃ XRD pattern. Our experimental pattern shows several peaks (indicated by arrows) with changes in position or intensity compared to the orthorhombic phase pattern. Thus, the splitting

peaks observed in the experimental XRD pattern are attributed to the interplanar spacing differences between the thick (stoichiometric CsPbBr₃) and thin (nonstoichiometric CsPbBr_{2.75}) nanobricks rather than an orthorhombic phase. It is concluded that the synthesized CsPbBr₃ nanobricks are a mixture of stoichiometric cubic CsPbBr₃ and nonstoichiometric CsPbBr_{2.75}. These results reveal a correlation between nanobrick thickness and the presence of Br vacancies. The nanobricks with a thickness of 10–20 nm exhibit a Br vacancy concentration of $\approx 8\%$, while those with a thickness of 50–60 nm show no detectable Br vacancies.

2.2. Degradation Behaviors of CsPbBr₃ Nanobricks under Electron Irradiation

The effect of thickness on the structural stability of CsPbBr₃ nanobricks was investigated by real-time TEM imaging. Previous literature suggests that the total electron dose is a key factor influencing the degradation of perovskite structures.^[43] Herein, electron dose rate is adopted as an important parameter to identify the stability of CsPbBr₃ nanobricks. Specifically, when the dose rate is below $500 \text{ e}^- \text{ \AA}^{-2} \text{ s}^{-1}$, the nanobricks are relatively stable. However, as the dose rate increases to $1250 \text{ e}^- \text{ \AA}^{-2} \text{ s}^{-1}$, significant degradation of CsPbBr₃ nanobricks occurs rapidly. This is attributed to the fact the high dose rate accelerates the degradation process. In addition, it is found that thick nanobricks appear to be more robust than thin ones. The thick CsPbBr₃ nanobricks last for $10 \approx 30 \text{ s}$ from initial formation of high-contrast nanoparticles to completion of the degradation process, while thin nanobricks decompose within seconds. Degradation behaviors differ between thick and thin CsPbBr₃ nanobricks. High-contrast nanoparticles first appear along the corners and edges of the thick nanobricks,

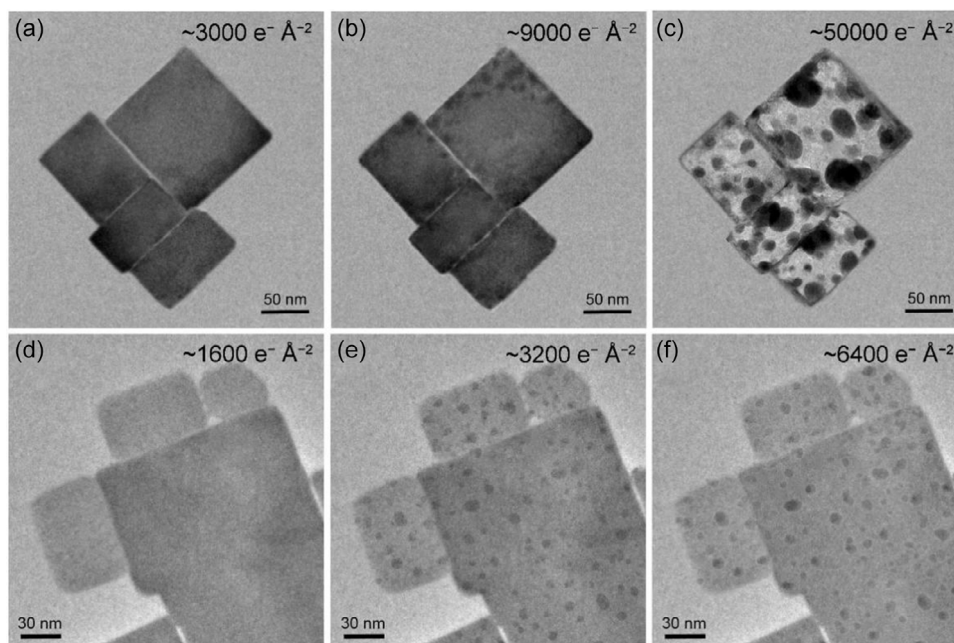


Figure 3. Typical BF TEM images of thick and thin CsPbBr₃ nanobricks in different states: a,d) undamaged, b,e) initially damaged, and c,f) fully decomposed.

as shown in Figure 3a,b. When decomposition is complete, as shown in Figure 3c, the thick nanobricks contain numerous voids and there are many large high-contrast nanoparticles. As for the thin nanobricks, Figure 3d,e shows that the damage takes place immediately, with many small high-contrast nanoparticles appearing randomly on surface. Upon further EB irradiation, some of the newly formed nanoparticles become blurred or even disappear (Figure 3f), without significant agglomeration. This is similar to previously reported degradation behaviors of CsPbBr₃ nanosheets.^[22] The high degradation rate of thin nanobricks may be attributed to the fact that bromine vacancies provide a greater number of undercoordinated atoms, decreasing the dissociation energy of atoms from the CsPbBr₃ lattice. It has been reported that Br vacancies in CsPbBr₃ (acting as negative-U centers) are favorable sites for Pb nanoparticle and Pb-Pb dimer formation.^[44]

To further explain the different degradation processes in thin and thick nanobricks, we acquired HRTEM images and EDS spectra to characterize the corresponding decomposition products. The resultant high-contrast nanoparticles observed in BF TEM image (Figure 4a) can be identified as metal Pb with a cubic structure ($a = 4.95 \text{ \AA}$) from the HRTEM images in Figure 4b. The interplanar spacing in particle A is measured to be

2.84 \AA , which is consistent with the interplanar spacing of {111} planes for cubic Pb. In addition, the angle between two planes is about 109.5° , which matches the angle between {111} planes of Pb. The lattice spacing in particle B is measured to be 2.45 \AA , corresponding to the (200) crystal plane of Pb. The HRTEM images here provide further evidence for the generation of Pb nanoparticles. Although $\text{Br}^- \rightarrow \text{Br}^0$ and $\text{Pb}^{2+} \rightarrow \text{Pb}^0$ transformations during decomposition have previously been reported,^[24] products other than Pb nanoparticles have not been clearly identified, especially the final state of Cs atoms. In Figure 4b, there are many low-contrast nanoparticles (enclosed by dashed lines) scattered around the high-contrast Pb nanoparticles. The interplanar spacing of these low-contrast nanoparticles is measured to be 3.04 \AA , corresponding to the {110} plane of CsBr ($a = 4.29 \text{ \AA}$). This indicates that crystalline CsBr is formed alongside Pb nanoparticles. The generation of Pb and CsBr is further supported by spectroscopic characterization of the nanobricks before and after decomposition. Quantification analysis of EDS spectra is presented in Table 1. The Cs/Pb atomic ratio (1.18:1) remains unchanged under EB irradiation, while the atomic ratio for Br/Pb changes from 2.98:1 to 0.66:1, indicating a drastic decrease in Br atomic percentage. Considering the inevitable Br loss during the acquisition of EDS spectra, the residual

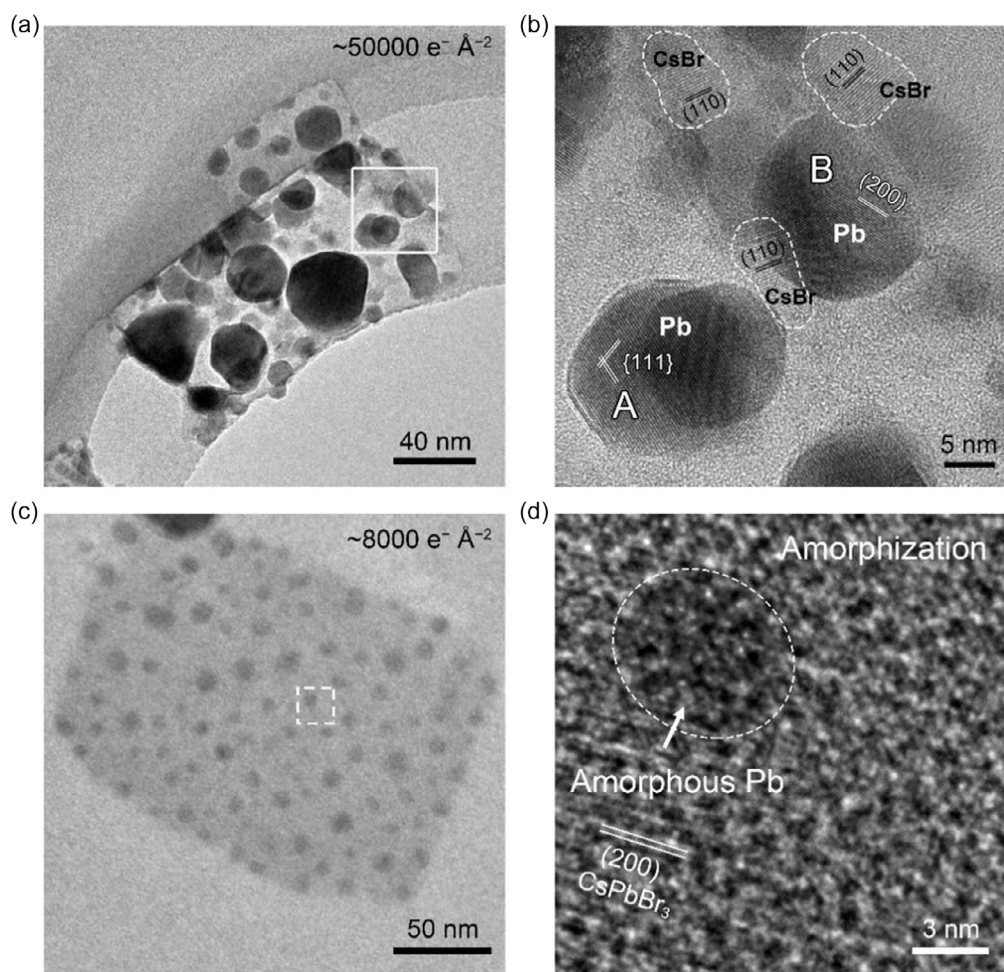


Figure 4. Decomposition products of CsPbBr₃ nanobricks under EB irradiation: a,b) thick CsPbBr₃ nanobricks; c,d) thin CsPbBr₃ nanobricks.

Table 1. Quantification analysis of EDS spectra from thick CsPbBr₃ nanobricks before and after decomposition under EB irradiation.

Composition	Weight percentage [%]		Atomic percentage [%]		Atomic ratio	
	Before	After	Before	After	Before	After
Cs	26.10	37.60	22.90	41.60	1.18	1.18
Pb	34.50	49.80	19.40	35.30	1.00	1.00
Br	39.60	12.60	57.70	23.20	2.98	0.66

Cs/Br atomic ratio is approximate to 1:1, consistent with the stoichiometry of CsBr. However, CsBr nanoparticles are only observed in thick nanobricks, suggesting that thickness plays an important role. Unlike the nanoparticles formed from thick nanobricks, the blurred nanoparticles formed from thin nanobricks (Figure 4c) appear to be largely amorphous. This is further confirmed by the HRTEM image in Figure 4d. The amorphization of newly formed, high-contrast Pb nanoparticles is thought

to be induced by EB irradiation.^[22] The surrounding low-contrast amorphous region might consist of Cs and Br atoms. This EB-induced amorphization is specific to thin nanomaterials such as 3 nm-thick nanosheets^[22] and the thin nanobricks in this work; the thick nanobricks (50 ≈ 60 nm) contain enough material to support the growth of large and stable Pb nanoparticles as well as CsBr nanoparticles.

Due to the extremely rapid degradation of thin nanobricks, we chose to use thick CsPbBr₃ nanobricks for detailed examination of structural evolution during the degradation process. Figure S6 (Supporting Information) shows time-resolved TEM images of morphological evolution in an individual thick nanobrick. High-contrast nanoparticles first appear along the corners and edges of thick CsPbBr₃ nanobricks after 10 s of irradiation, which is attributed to the fact that edge atoms are under-coordinated and more easily activated. As irradiation continues, the number and size of nanoparticles increase rapidly. When the nanoparticles reach a critical size, the surrounding nanobrick regions are destroyed and voids appear. The voids spread very fast

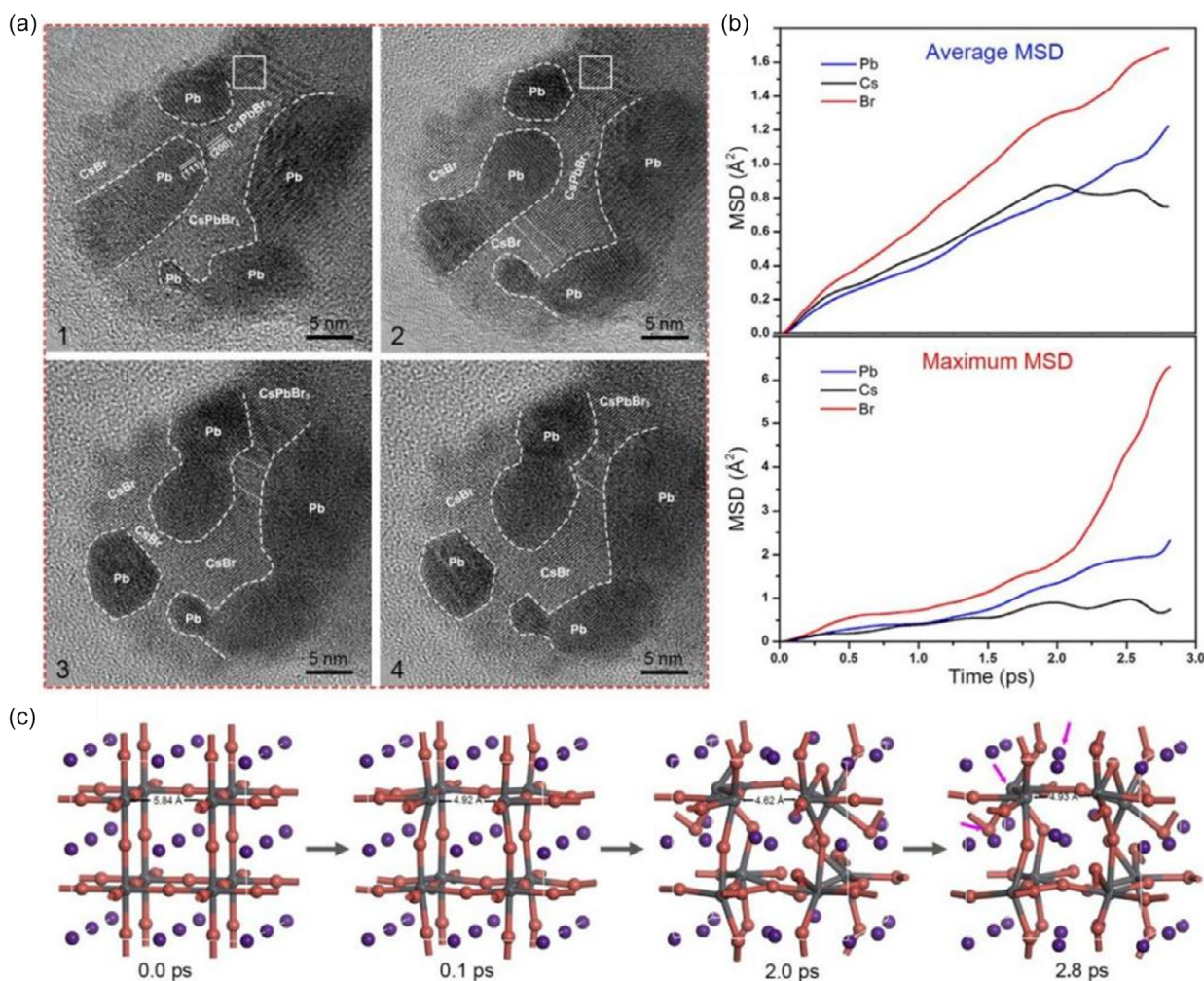


Figure 5. a) Time-resolved microstructure evolution of CsPbBr₃ under EB irradiation (dose rate: ≈2000 e⁻ Å⁻² s⁻¹). The time interval between successive image acquisitions is 2 s. b) Ab initio molecular dynamics (AIMD) simulations of the CsPbBr₃ supercell after losing one Br atom: the top image is for all Cs, Pb, and Br atoms and the bottom image is for Cs, Pb, and Br atoms with the maximum displacements as marked with purple arrows in (c); c) time-resolved structural models of CsPbBr₃.

and the perovskite lattices collapse very quickly, resulting in rapid degradation of CsPbBr_3 . After 22 s, the decomposition process of CsPbBr_3 nanobricks is almost complete. Subsequently, the high-contrast nanoparticles undergo constant migration and rearrangement to maintain thermodynamic stability under further EB irradiation.

The dynamic variation of chemical composition is reflected by microstructural evolution during nanobrick breakdown. **Figure 5a** shows time-resolved (time interval: 2 s) HRTEM images obtained from an individual CsPbBr_3 nanobrick after appearance of high-contrast Pb nanoparticles. Upon closer examination of **Figure 5a**, it is evident that the image contrast evolves over time, signifying the gradual degradation of CsPbBr_3 . In addition, careful observation of **Figure 5a-1** reveals variations in contrast among different regions, implying diverse material compositions. Furthermore, the interplanar spacings are measured from the image to identify the different species, as demonstrated in **Figure 5a**. The regions enclosed by dashed lines delimit newly formed Pb nanoparticles. The evolution processes of CsPbBr_3 , CsBr, and Pb phases can be observed. From **Figure 5a-1**, we observe an epitaxial orientation relationship of $[001]_{\text{CsPbBr}_3} // [1-10]_{\text{Pb}}$ and $\{200\}_{\text{CsPbBr}_3} // \{111\}_{\text{Pb}}$ which demonstrates that Pb^0 atoms, once transformed from Pb^{2+} ions, migrate out of the parent CsPbBr_3 lattice and gather together

to form Pb nanoparticles. The contrast variation observed in regions enclosed by white solid lines in **Figure 5a-1,2** indicates Br loss from CsPbBr_3 . This is analogous to the occurrence of oxygen vacancies in BiMnO_3 induced by EB irradiation.^[45] Subsequently, the perovskite lattice collapses, and dissociated Br atoms are stabilized by the remaining Cs atoms to form CsBr nanocrystals around Pb nanoparticles, as shown in **Figure 5a-3,4**. The formation of CsBr nanocrystals leads to the appearance of voids (**Figure S5**, Supporting Information). We ascribe this to lattice shrinkage due to the smaller lattice constant of CsBr compared to CsPbBr_3 . The epitaxial relationship between Pb nanoparticles and the parent lattice gradually degrades. Upon further EB irradiation, dynamic microstructural evolution and deformation of Pb nanoparticles are observed, implying a continuous Pb lattice reconfiguration. This is attributed to thermal effects and the specific crystal structure of Pb. Some degree of heating is inevitable when the EB interacts with the specimen, especially for materials with poor thermal conductivity.^[19] Pb has better thermal conductivity than CsBr, but thermal susceptibility is also affected by the crystal structure of materials. Pb and CsBr have different structures, the former being face-centered cubic (fcc) and the latter being body-centered cubic (bcc). The fcc crystals possess more slip systems, leading to increased plastic deformation. Consequently, in the presence of accumulated

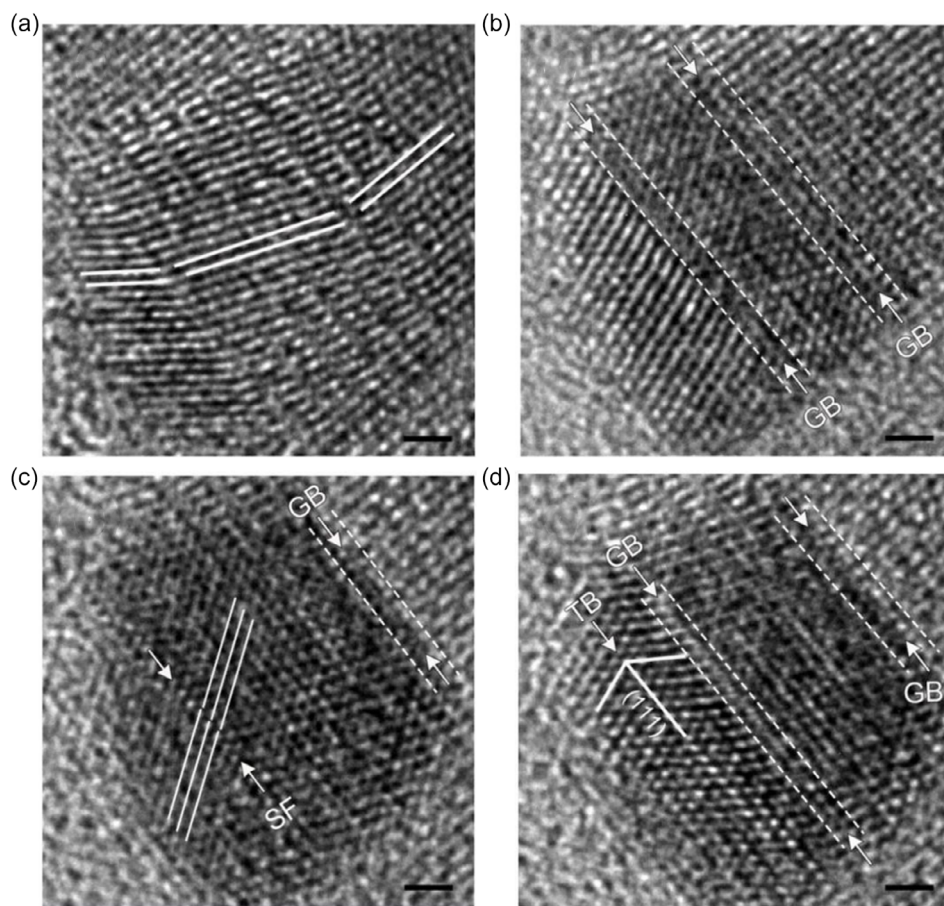


Figure 6. a–d) Formation of a stacking fault and twinning during lattice rearrangement of a Pb nanoparticle. The time interval for image acquisition is 2 s and the dose rate is $\approx 2000 \text{ e}^- \text{ \AA}^{-2} \text{ s}^{-1}$. The scale bar is 1 nm.

thermal energy, Pb nanocrystals are more prone to continual lattice reconstruction.

AIMD simulation was implemented for a $2 \times 2 \times 2$ CsPbBr₃ supercell with one bromine vacancy to further explore the dynamic structural evolution of CsPbBr₃ after losing Br atoms. It is exceedingly difficult to reconstruct a complete degradation process using AIMD simulations because of difficulty in modeling atomic motion within the supercell. Instead, a very short time interval (just 2.8 ps) was chosen to focus on the initial degradation phase only. The calculated average mean-squared displacement (MSD) of all Cs, Pb, and Br atoms (Figure 5b) indicates that the loss of Br atoms makes the supercell thermodynamically unstable and triggers the degradation of CsPbBr₃. The initial MSDs for Cs, Pb, and Br atoms increase quickly, confirming that the degradation process is fast. After 2 ps, Cs atoms tend to reach equilibrium, while Pb and Br atoms continue to move, increasing their opportunity to escape from the lattice. In addition, the MSD of maximally displaced Br atoms is much larger than the average MSD. We infer that a fraction of Br atoms is constrained by Cs atoms, as expected. Figure 5c illustrates structural evolution during the dynamic process. We conclude that the two Pb atoms adjacent to a bromine vacancy move toward each other until the distance between them is less than 4.93 Å (close to the lattice parameter of metallic Pb), where a new equilibrium state is attained. These results provide additional evidence for our proposed degradation mechanism of CsPbBr₃.

Under persistent EB irradiation, atomic rearrangements occur continuously in the Pb nanocrystals. During the atomic rearrangement process, numerous crystal defects (including dislocation and twinning) are observed. A typical HRTEM image of the

misfit dislocation (D) is presented in Figure S7a (Supporting Information). The Burgers vector for the D is determined to be $1/2 \langle 110 \rangle$. The grain and twin boundaries in the Pb nanoparticle are illustrated in Figure S7b (Supporting Information). The grain boundary is marked as GB and the twin boundary is labeled as TB. The lattice spacing is measured to be 2.82 Å, corresponding to the (111) plane. The microstructural evolution of the Pb crystal is recorded, as shown in Figure 6. Due to the weak bonding of edge atoms, the Pb⁰ seed crystal preferentially forms at the corner of the nanobrick, as shown in Figure 6a. The Pb⁰ seed then grows into nanoparticle, with accumulation of Pb⁰ atoms originating from the parent CsPbBr₃ nanobrick. The resulting Pb nanoparticle is still bound to the initial lattice and restricted by its boundary. Cumulative stress drives the lattice planes to bend as depicted by white lines in Figure 6a and triggers the formation of new grain boundaries in the growing Pb nanoparticle, as shown in Figure 6b. Residual stress can induce further reconstruction of Pb nanoparticles, resulting in the high-energy stacking fault seen in Figure 6c. Meanwhile, energy from continuous EB irradiation continues to accumulate. The GB and TB form to release excess energy from the system, as shown in Figure 6d.

Based on the above results, Figure 7 proposes a plausible mechanism for the degradation of CsPbBr₃ nanobricks with different thicknesses under EB irradiation. As shown in Figure 7a, damage in thick nanobricks starts preferentially at corners or edges where there are many dangling bonds and under-coordinated Pb atoms. The degradation process starts at the outside and proceeds toward the center of thick nanobricks. At first, the bonding of Br atoms to adjacent Pb atoms is broken by knock-

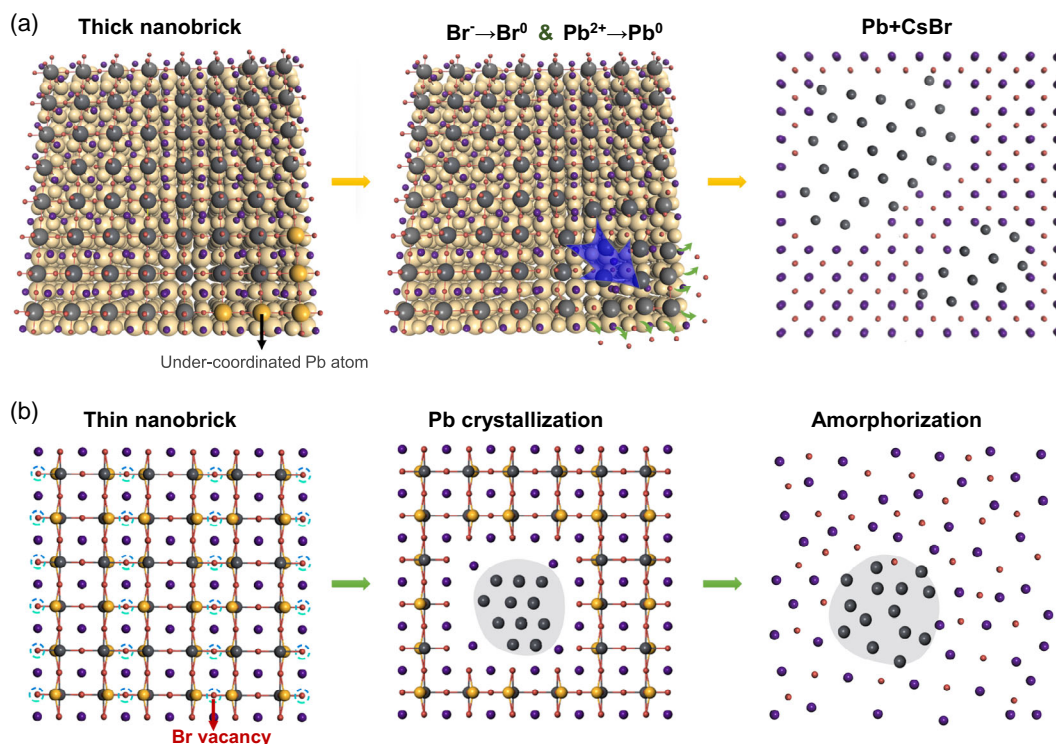


Figure 7. a) Schematic diagrams of the decomposition process in thick and b) thin CsPbBr₃ nanobricks under EB irradiation.

on collisions of electrons with high incident energy. Br atoms escape the lattice to form Br₂ (the oxidation of Br⁻), leaving numerous bromine vacancies in the lattice. Knock-on collisions play a dominant role at this stage. To lower the defect states of bromine vacancies, adjacent Pb atoms tend to approach each other,^[46] providing an opportunity to form a Pb seed crystal. This phenomenon is more visible in thin nanobricks (Figure 7b). Under further irradiation, the Pb seed crystal tends to migrate out of the lattice along vacancies to form Pb nanoparticles (the reduction of Pb²⁺). The process relies on two key phenomena. First, due to the formation of bromine vacancies, numerous Pb atoms become undercoordinated^[47] and their diffusion energy decreases significantly. Second, bromine vacancies provide channels for Pb seed crystals to agglomerate and migrate out of the lattice. Continuous thermal accumulation in the newly formed Pb nanoparticles under EB irradiation induces agglomeration and lattice rearrangement. Pb and Br deficiencies imply the destruction of PbBr₆⁴⁻ octahedra, which are the support structure of the CsPbBr₃ lattice, leading to complete lattice collapse. Meanwhile, a fraction of Br atoms is captured by Cs atoms to form CsBr. In the case of thin nanobricks, bromine vacancies within the crystal lattice provide more active sites for Pb diffusion and become the origin of structural damage, leading to rapid formation of small Pb nanoparticles at random locations in the nanobrick. Upon further EB irradiation, the resultant Pb nanocrystal is fragmented and transformed to amorphous Pb⁰ which spreads out onto the supporting carbon film. With the framework collapsed, an amorphous structure composed of Cs and Br appears; there are no longer sufficient Cs and Br atoms in the ultrathin CsPbBr₃ nanobrick to form a stable CsBr nanocrystal. The different transformation behaviors of thick and thin nanobricks are therefore ascribed to their inherent crystal structure and thickness.

3. Conclusion

In summary, CsPbBr₃ nanobricks with different thicknesses have been synthesized by a hot-injection method. Thick nanobricks exhibit better stability than thin ones under EB irradiation. The different EB-induced transformations in thick and thin nanobricks are caused by thickness-dependent microstructural dynamics. A modulated crystal structure observed in thin nanobricks indicates that bromine vacancies become ordered along a particular direction, as confirmed by further study of experimental and simulated electron diffraction patterns. Bromine vacancies provide a large number of under-coordinated Pb atoms which facilitate the degradation of CsPbBr₃ under EB irradiation. Progressive irradiation damage of CsPbBr₃ nanobricks involves the oxidation of Br⁻ to Br₂, the reduction of Pb²⁺ to Pb⁰, and the formation of CsBr. A continuous lattice rearrangement coinciding with the formation and growth of crystal defects is observed in newly formed Pb nanoparticles, driven by EB irradiation. Although CsPbBr₃ nanocrystals are highly defect-tolerant with respect to their optoelectronic properties, bromine vacancies have a great impact on their structural stability. Our work suggests a possible strategy for the development of defect-free lead halide perovskites *via* careful control of their thickness. An improved understanding of EB-induced damage in CsPbX₃

materials will contribute to future characterization and development of these materials.

4. Experimental Section

Chemical Reagents: Cs₂CO₃ (99.9%), PbBr₂ (99.0%), oleic acid (OIAc, 90%), oleylamine (OIAm, 90.0%), octadecene (ODE, 90.0%), octanoic acid (OctAc, 99.0%), octylamine (OctAm, 99.5%), and hexane were purchased from Aladdin and used without any further purification.

Preparation of Cs-Oleate Precursor Solution: The Cs-oleate precursor solution was prepared by loading 0.13 g of Cs₂CO₃ and 20 mL of OIAc into a 100 mL three-neck flask. The mixture was then stirred for 1 h at 100 °C under vacuum. Finally, the solution was heated to 150 °C under N₂ until Cs₂CO₃ reacted with OIAc completely and a brownish-red Cs-oleate solution was obtained.

Synthesis of CsPbBr₃ Nanobricks: CsPbBr₃ nanobricks were synthesized using a hot-injection approach^[25] with slight modifications. 10 mL of ODE, 1.25 mL of OIAc, 1.25 mL of OIAm, 1.25 mL of OctAc, 1.25 mL of OctAm, and 0.13 g of PbBr₂ were degassed at 100 °C for 30 min in a 100 mL three-neck flask. Then, the solution was heated to 200 °C under a N₂ atmosphere for 30 min to completely solubilize PbBr₂, followed by a rapid injection of 5 mL of Cs-oleate solution. After 5 min, the suspension was cooled to room temperature using a water bath. 10 mL of hexane was added to the suspension, and the mixture was centrifuged at 700 rpm for 5 min. After centrifugation, the supernatant was discarded and the nanobricks were dispersed in hexane for further characterization.

Characterization: A Rigaku SmartLab XRD with Cu-K_α radiation ($\lambda = 1.5406 \text{ \AA}$) was used to profile the crystal structures. BF TEM imaging, HRTEM, SAED analyses, and EDS were performed on a JEOL JEM 2100F transmission electron microscope operating at 200 kV. The total electron dose for EDS spectrum acquisition was $\approx 4500 \text{ e}^- \text{ \AA}^{-2}$. The composition of the nanobricks was determined from the EDS spectra using the Cliff-Lorimer approximation method, involving fitting of the Cs L_α, Pb L_α, and Br K_α lines. AFM measurements were conducted using an MFP-3D Origin atomic force microscope under a nitrogen atmosphere. EELS spectra were performed on probe-corrected FEI G2 80-200 S/TEM operating at 200 kV. The EELS spectra were obtained in STEM mode with a semi-convergence angle of 21 mrad and a collection angle of 62 mrad.

Computational Methodology: DFT calculations were used to geometrically optimize CsPbBr₃ atomic models using the DMol³ program package in Materials Studio. The generalized gradient approximation with the Perdew–Burke–Ernzerhof functional was used to calculate the exchange-correlation energy. Atomic valence-band orbitals were described using the double-numeric polarization basis set, and core electrons were replaced by DFT semicore pseudopotentials. Energy and displacement convergence criteria for structure optimization were set to 2.0×10^{-5} Hartree per atom and 0.005 Å, respectively. To investigate the degradation behavior of CsPbBr₃, AIMD treated by the canonical ensemble (NVT) was carried out on a $2 \times 2 \times 2$ supercell using the CASTEP program package. The AIMD simulation was performed at room temperature (300 K), lasting 2800 steps with a time step of 1 fs. Theoretical electron diffraction and X-ray powder diffraction patterns were generated from the optimized atomic models using CrystalMaker Software.

Supporting Information

Supporting Information is available from the Wiley Online Library or from the author.

Acknowledgements

The authors would like to thank the financial support from high-end foreign experts project of the Ministry of Science and Technology, China (grant no. G2022025015L, G2022025016L), the Shandong Province “Double-Hundred Talent Plan” (grant No. WST2018006), and

the Top-notch Innovative Talent Program of Qingdao City, China (grant no. 13-CX-8). Y. Q. Wang would also like to thank the financial support from the Taishan Scholar Program of Shandong Province, China, Qingdao International Center of Semiconductor Photoelectric Nanomaterials, and Shandong Provincial University Key Laboratory of Optoelectrical Material Physics and Devices. F.R. is grateful to the Canada Research Chairs program for partial salary support. We would like to thank Mr. Joseph Parker from the University of Manchester, UK for English language improvement.

Conflict of Interest

The authors declare no conflict of interest.

Data Availability Statement

The data that support the findings of this study are available from the corresponding author upon reasonable request.

Keywords

bromine vacancies, CsPbBr₃ nanobricks, in situ transmission electron microscopy, microstructure, thicknesses

Received: December 27, 2023

Revised: March 5, 2024

Published online: March 19, 2024

- [1] X. Zhu, L. Ge, Y. Wang, M. Li, R. Zhang, M. Xu, Z. Zhao, W. Lv, R. Chen, *Adv. Opt. Mater.* **2021**, *9*, 2100058.
- [2] J. Song, J. Li, X. Li, L. Xu, Y. Dong, H. Zeng, *Adv. Mater.* **2015**, *27*, 7162.
- [3] J. Y. Y. Loh, G. Sharma, N. P. Kherani, G. A. Ozin, *Adv. Energy Mater.* **2021**, *11*, 2101566.
- [4] G. Al-Dainy, F. Watanabe, A. S. Biris, S. E. Bourdo, *ACS Appl. Energy Mater.* **2021**, *4*, 3297.
- [5] H. Chen, F. Zhou, Z. Jin, *Nano Energy* **2021**, *79*, 105490.
- [6] K. Chen, W. Jin, Y. Zhang, T. Yang, P. Reiss, Q. Zhong, U. Bach, Q. Li, Y. Wang, H. Zhang, Q. Bao, Y. Liu, *J. Am. Chem. Soc.* **2020**, *142*, 3775.
- [7] M. M. Byranvand, M. Saliba, *Sol. RRL* **2021**, *5*, 2100295.
- [8] Q. Zhang, F. Diao, X. Xue, X. Sheng, D. Barba, Y. Wang, *ACS Appl. Mater. Interfaces* **2021**, *13*, 44777.
- [9] H. Zhang, M. K. Nazeeruddin, W. C. H. Choy, *Adv. Mater.* **2019**, *31*, 1805702.
- [10] R. Bauld, L. M. Fleury, M. Van Walsh, G. Fanchini, *Appl. Phys. Lett.* **2012**, *101*, 103306.
- [11] Y. Gao, Y. Hu, C. Yao, S. Zhang, *Adv. Funct. Mater.* **2022**, *32*, 2208225.
- [12] S. Kundu, T. L. Kelly, *EcoMat* **2020**, *2*, e12025.
- [13] Z. Song, C. Wang, A. B. Phillips, C. R. Grice, D. Zhao, Y. Yu, C. Chen, C. Li, X. Yin, R. J. Ellingson, M. J. Heben, Y. Yan, *Sustainable Energy Fuels* **2018**, *2*, 2460.
- [14] Y. Liu, C. Xie, W. Tan, X. Liu, Y. Yuan, Q. Xie, Y. Li, Y. Gao, *Org. Electron.* **2019**, *71*, 123.
- [15] S. Li, J. Zhong, Z. Cui, Q. Zhang, M. Sun, Y. Wang, *J. Mater. Chem. C* **2019**, *7*, 13829.
- [16] P. P. Shanbogh, V. C. Petwal, J. Dwivedi, A. Rao, N. G. Sundaram, *J. Phys. Chem. C* **2019**, *123*, 10881.
- [17] Z. Yang, M. Walls, I. Lisiecki, M.-P. Pileni, *Chem. Mater.* **2013**, *25*, 2372.
- [18] Y. Yu, D. Zhang, C. Kisielowski, L. Dou, N. Kornienko, Y. Bekenstein, A. B. Wong, A. P. Alivisatos, P. Yang, *Nano Lett.* **2016**, *16*, 7530.
- [19] Y.-H. Seo, J. H. Kim, D.-H. Kim, H.-S. Chung, S.-I. Na, *Nano Energy* **2020**, *77*, 105164.
- [20] J. A. Sichert, Y. Tong, N. Mutz, M. Vollmer, S. Fischer, K. Z. Milowska, R. García Cortadella, B. Nickel, C. Cardenas-Daw, J. K. Stolarczyk, A. S. Urban, J. Feldmann, *Nano Lett.* **2015**, *15*, 6521.
- [21] R. F. Egerton, *Microsc. Res. Tech.* **2012**, *75*, 1550.
- [22] Z. Dang, J. Shamsi, F. Palazon, M. Imran, Q. A. Akkerman, S. Park, G. Bertoni, M. Prato, R. Brescia, L. Manna, *ACS Nano* **2017**, *11*, 2124.
- [23] Z. Dang, J. Shamsi, Q. A. Akkerman, M. Imran, G. Bertoni, R. Brescia, L. Manna, *ACS Omega* **2017**, *2*, 5660.
- [24] L. Zhang, L. Liu, P. Zhang, R. Li, G. Zhang, X. Tao, *ACS Appl. Mater. Interfaces* **2020**, *12*, 39834.
- [25] X. Liu, S. Li, Z. Li, Y. Zhang, W. Yang, Z. Li, H. Liu, D. V. Shtansky, X. Fang, *Adv. Funct. Mater.* **2021**, *31*, 2101480.
- [26] Y. Zhang, F. Cao, S. Li, X. Liu, L. Kang, L. Wu, X. Fang, *J. Mater. Sci. Technol.* **2022**, *129*, 108.
- [27] Y. Zhang, S. Li, Z. Li, H. Liu, X. Liu, J. Chen, X. Fang, *Nano Lett.* **2021**, *21*, 382.
- [28] Y. Zhang, J. Yao, Z. Zhang, R. Zhang, L. Li, Y. Teng, Z. Shen, L. Kang, L. Wu, X. Fang, *J. Mater. Sci. Technol.* **2023**, *164*, 95.
- [29] R. K. Behera, S. Bera, N. Pradhan, *ACS Nano* **2023**, *17*, 7007.
- [30] W. Zheng, X. Xiong, R. Lin, Z. Zhang, C. Xu, F. Huang, *ACS Appl. Mater. Interfaces* **2018**, *10*, 1865.
- [31] M. Zhang, Z. Zheng, Q. Fu, Z. Chen, J. He, S. Zhang, L. Yan, Y. Hu, W. Luo, *CrystEngComm* **2017**, *19*, 6797.
- [32] Y. Liu, Y. Li, X. Hu, C. Wei, B. Xu, J. Leng, H. Miao, H. Zeng, X. Li, *Chem. Eng. J.* **2023**, *453*, 139904.
- [33] D. Yan, T. Shi, Z. Zang, T. Zhou, Z. Liu, Z. Zhang, J. Du, Y. Leng, X. Tang, *Small* **2019**, *15*, 1901173.
- [34] Y. Bekenstein, B. A. Koscher, S. W. Eaton, P. Yang, A. P. Alivisatos, *J. Am. Chem. Soc.* **2015**, *137*, 16008.
- [35] M. C. Brennan, M. Kuno, S. Rouvimov, *Inorg. Chem.* **2019**, *58*, 1555.
- [36] B. Liu, G. Liu, H. Feng, C. Wang, H. Yang, Y. Wang, *Mater. Des.* **2016**, *89*, 715.
- [37] J.-H. Kwon, W. S. Choi, Y.-K. Kwon, R. Jung, J.-M. Zuo, H. N. Lee, M. Kim, *Chem. Mater.* **2014**, *26*, 2496.
- [38] Y.-M. Kim, J. He, M. D. Biegalski, H. Ambaye, V. Lauter, H. M. Christen, S. T. Pantelides, S. J. Pennycook, S. V. Kalinin, A. Y. Borisevich, *Nat. Mater.* **2012**, *11*, 888.
- [39] R. Brescia, S. Toso, Q. Ramasse, L. Manna, J. Shamsi, C. Downing, A. Calzolari, G. Bertoni, *Nanoscale Horiz.* **2020**, *5*, 1610.
- [40] F. Bertolotti, G. Nedelcu, A. Vivani, A. Cervellino, N. Masciocchi, A. Guagliardi, M. V. Kovalenko, *ACS Nano* **2019**, *13*, 14294.
- [41] H. Feng, Y. Wang, C. Wang, F. Diao, W. Zhu, P. Mu, L. Yuan, G. Zhou, F. Rosei, *Nanotechnology* **2016**, *27*, 295703.
- [42] J. Shamsi, Z. Dang, P. Bianchini, C. Canale, F. Di Stasio, R. Brescia, M. Prato, L. Manna, *J. Am. Chem. Soc.* **2016**, *138*, 7240.
- [43] X.-G. Zhou, C.-Q. Yang, X. Sang, W. Li, L. Wang, Z.-W. Yin, J.-R. Han, Y. Li, X. Ke, Z.-Y. Hu, Y.-B. Cheng, G. Van Tendeloo, *J. Phys. Chem. C* **2021**, *125*, 10786.
- [44] J. Kang, J. Li, S.-H. Wei, *Appl. Phys. Rev.* **2021**, *8*, 031302.
- [45] H. Yang, Z. H. Chi, F. Y. Li, C. Q. Jin, R. C. Yu, *Phys. Rev. B* **2006**, *73*, 024114.
- [46] H. Shi, M.-H. Du, *Phys. Rev. B* **2014**, *90*, 174103.
- [47] K. Hills-Kimball, H. Yang, T. Cai, J. Wang, O. Chen, *Adv. Sci.* **2021**, *8*, 2100214.